

Anisotropic optical conductivities of Model Topological nodal-line Semimetals

Sita Kandel^{1,2}, Godfrey Gumbs^{1,2,3}, and Oleg L. Berman^{2,4}

¹*Department of Physics, Hunter College, City University of New York, 695 Park Avenue, New York, NY 10065 USA*

²*The Graduate School and University Center, The City University of New York, New York, NY 10016, USA*

³*Donostia International Physics Center (DIPC), P de Manuel Lardizabal,
4, 20018 San Sebastian, Basque Country, Spain and*

⁴*Physics Department, New York City College of Technology,
The City University of New York
Brooklyn, NY 11201 USA*

(Dated: October 16, 2023)

With the use of simple models, we investigated the optical conductivity of a nodal-line semimetal (NLSM) whose crossing of the conduction and valence bands near the origin (O point) in the (k_x, k_y) plane of a small cubic region can be adjusted by a parameter α . The Hamiltonian of the NLSM is based on the $\mathbf{k} \cdot \mathbf{p}$ model for the low-lying energy bands. When $\alpha = 0$, these bands touch each other along a continuous closed loop but the opening of a band gap corresponding to finite values of α and the varying of the carrier concentration can be adjusted. This provides a tunable semiconductor gap, around the O point and the valence and conduction bands can meet at a pair of points within the small cubic region in \mathbf{k} space. The optical conductivity of such a NLSM is calculated using the Kubo formula with emphasis on the optical spectral weight redistribution, deduced from appropriate Green's functions, brought about by changes in gap and chemical potential due to modifying α . We derived closed-form semi-analytic expressions for the longitudinal components of the optical conductivity for these model systems of NLSM and compare results for chosen α and chemical potential. We also present results for the heat capacity when the system is in thermal equilibrium for various chosen α and chemical potential.

Corresponding Author: Oleg L. Berman, Email: OBerman@citytech.cuny.edu.

I. INTRODUCTION

Topological semimetals (TSM) have been emerging as a fast growing group of topological materials which have been coming under increasing scrutiny.¹⁻³ For these systems, the conduction and valence bands cross each other in the Brillouin zone. It is important to note that the crossing cannot be eliminated by perturbing the Hamiltonian without breaking either its crystalline or time-reversal symmetry. For Dirac semimetals, the conduction and valence bands have linear crossing at the Dirac point. If the time reversal symmetry is broken, the Dirac point splits into two separate ones, and the system becomes a Weyl semimetal. On the other hand, for the nodal-line semimetal (NLSM), the crossing of the valence and conduction bands forms a nodal ring (also called nodal line). There is a significant difference in the density-of-states near the Fermi surface between the NLSM compared to Dirac and Weyl semimetals. Due to the linear energy dispersion, the density-of-states of Dirac and Weyl semimetals is linear in energy and vanishes at the Fermi level. We do not find this behavior in our model of NLSM. For 3D TSM, two bands may cross one another at discrete points or along a closed curve.

For a TSM, one can associate for each band crossing a topological invariant which depends on the symmetry group that protects the nodal structure. Various material systems have been proposed as NLSM protected by different symmetry groups. For example, TaAs⁴ has been shown to be a NLSM protected by mirror reflection and spin rotation symmetries with two nodal lines in the absence of spin orbital coupling (SOC). However, in the presence of SOC, each nodal line is grouped into three pairs of Weyl nodes. SrIrO₃⁵ is another NLSM with a double nodal line. This material is separated into a pair of Dirac nodes under broken mirror reflection symmetry.

For many years, the topological phases of matter, topological insulators and topological semimetals, both Dirac and Weyl semimetals, have been widely studied theoretically and experimentally. When it came to be known that some topological semimetals exhibit different dispersion relations than that of Dirac and Weyl, making a nodal ring at the cross-section of valence and conduction bands, NLSM have attracted tremendous interest in condensed matter physics. The optical conductivity of NLSM has also been studied both theoretically and experimentally⁶⁻¹⁶. For example, in 2016/17, Carbotte and his team^{6,7} studied the optical response of such NLSM as a function of different parameters using the Kubo formula. They presented analytical and numerical solutions for the optical conductivity of a NLSM using a toy model Hamiltonian. They came to the conclusion that their 3D NLSM presents 2D Dirac-like response in the low-photon energy regime and 3D Dirac-like response in the high-energy photon limit, i.e. the

optical conductivity is increased linearly with photon frequency. Later on in 2017, Barati⁸ also showed that the optical conductivity of NLSM is anisotropic. The response along the direction parallel to the plane containing the nodal ring increases linearly while that along the direction perpendicular to the nodal ring saturates to constant value at high frequencies. Both those authors considered different toy models in order to explain NLSM with different Fermi surface. However, neither of these results totally agree with the paper by Habe and Koshino⁹ in 2018. Koshino and his team studied theoretically the dynamical conductivity of NLSM ZrSiS by using a multi-orbital tight-binding model based on a first-principles energy band calculation. According to Habe and Koshino, for ZrSiS type NLSM, the interband contribution first increases slowly for some frequency range and is decreased to smaller value and saturates for large frequency.

More advanced and very sophisticated model Hamiltonians have been used to capture the behavior of properties of materials with line nodes. For instance, the authors in Ref. [10] have considered a heterostructure which is in a topological semimetallic phase with line nodes. By employing the Kubo formula, they have investigated the dependence of the dc conductivity on magnetization M for a structure consisting of alternate layers of topological insulators where spin splitting, resulting from magnetization in the z direction was included. Also tunneling within a topological insulator layer and between neighboring topological insulator layers was also taken into consideration and explicitly contribute to the model Hamiltonian that displays a number of anomalous properties and possess novel correlated phases. The dependence of the dispersion on the strength of the time-reversal breaking plays a crucial role in this model. Likewise, the paper by Yan, et al.¹⁷ deals with the collective modes of nodal line semimetals. With their model Hamiltonian, they were able to obtain the plasmon dispersion relation which in the regime of modest doping and in the long wavelength limit, the frequency of the mode was shown to obey $\omega_p \sim n^{1/4}$ where n is the carrier density. This is in contrast with ordinary electron liquids and the Dirac-Weyl liquids. But, in the regime of very low doping the $\omega_p \sim n^{1/4}$ law crosses over to $\omega_p \sim n^{1/2}$. These calculations were done in the random-phase approximation with the polarization function determined using a bubble consisting of single-particle Green's functions without self-energy corrections.

This brief overview has motivated us to study the optical response of materials similar to Dirac semimetal and Weyl semimetal using a simple model Hamiltonian in conjunction with the Kubo formula which yields semi-analytic results for the optical conductivity. Our results include contributions from both intra and interband transitions between the low-energy subbands for our model Hamiltonian. The obtained results are interesting because the numerical solutions have similar features to Habe and Koshino's results⁹ and are neither like 2D nor 3D Dirac or Weyl semimetal. The transverse optical conductivity of NLSM is found to vanish due to rotational symmetry along the ring of NLSM. This result is also supported by a recent study of Wang¹¹, who demonstrated the anomalous Hall optical conductivity in tilted topological NLSM. We refer to Ref. [18] for a review of other remarkable properties of these TSM systems as well as a discussion of possible technological applications. The optical conductivity of monolayer and bilayer graphene, and few-layer epitaxial graphite has been reported recently¹⁹. These studies have yielded useful information regarding the electron dynamics and this is a plausible reason for our present investigation into NLSM. Here, we consider the optical conductivity of a NLSM model system with special emphasis on the optical spectral weight redistribution due to changes in the chemical potential caused by charging as well as an adjustable parameter α which governs the degree of crossing or the gap between the valence and conduction bands. The doping determines the position of the Fermi level which could be located within the energy gap or the conduction sub band. The parameter α can be manipulated by strain and the doping could be varied through the intercalation of donor atoms or by applying a voltage to metal gate. The effect of mechanical strain on the optical properties of NLSM ZrSiS has been studied using first-principles calculations in Ref. [12]. According to Ref. [12], frequency-independent optical conductivity is robust with respect to uniaxial compressive strain of up to 10 GPa. Therefore, our reported studies related to the possible control of the optical conductivity of a model NLSM system by external strain is likely to attract attention from theoretical and experimental researchers.

It is also worthy of note that for slabs of finite thickness unusual surface states, Fermi-arc surface states in Weyl semimetal^{20,21}, and drumhead surface states in NLSM^{1,22-26} are supported by TSM. So far, only bulk and surface Landau levels, together with their transport properties, have been extensively investigated for Dirac semimetal²⁷⁻³¹ and Weyl semimetal³²⁻³⁷. We emphasize that in this paper, we consider only a bulk NLSM. However, we may model the effects due to a surface by a slab containing multi-layers of single atoms with two orbitals and stacked one on top the other along a specific direction. The surface states of topological materials are significantly affected by the number of layers and impurities. When the number of material layers is insufficient, the surface state will not be formed, or impurities in the system can readily destroy the surface states. In general, observation of surface states of topological materials such as drumhead surface states of NLSM^{1,22-26} is still a great challenge. Our current work mainly focuses on the physical properties of bulk states.

The rest of this paper is organized as follows. In Sec. II, we present a continuum model Hamiltonian for low-energy subbands based on the $\mathbf{k} \cdot \mathbf{p}$ method. These energy bands are displayed within a small cubic region. We also present

the theoretical formalism for calculating the optical conductivity based on this simple Hamiltonian. This model involves an adjustable parameter α associated with a nodal circle which may shrink to a point when $\alpha = 0$. Here, we have managed to derive a conveniently simple semi-analytical expression for the frequency-dependent conductivity for arbitrary chemical potential, making this a convenient result for experimentalists to explore further. In Sec. III, we present numerical results demonstrating the anisotropy of the system, the α -dependence and charging pertaining to the biasing of the NLSM sample. In Sec. IV, we present and discuss our numerical results for the density-of-states. Acknowledging that the Hamiltonian in Sec. II is not fully representative of the band structure properties of a specific NLSM but only captures some essential properties of this class of materials, we present another model Hamiltonian in Sec. V. We discovered that both models have similar behaviors for their optical conductivities and so may be employed to make some important predictions about the optical properties of NLSMs. We present in Sec. VI numerical results for the heat capacity of a NLSM in thermal equilibrium. The formalism is rather straightforward and makes use of the grand potential. Section VII is devoted to a summary of our results. Some of the algebraic calculations are presented in appendices.

II. THEORETICAL BACKGROUND

Let us consider a Hamiltonian for which the nodal line is stable against perturbations. However, the nodal line may still shrink continuously to a point. In this regard, we turn to a single-spin effective Hamiltonian of a material such as ZrSiSe and ZrSiTe.^{2,3} In Ref. [1], the band structure of ZrSiTe was obtained using *ab initio* calculations. The idea here is to carry out a calculation based on a model Hamiltonian which mimics the essential features of the true band structure near the Γ point of a NLSM such as ZrSiTe. In general, these band structures obtained from first-principles calculations or the generalized tight-binding model are very complicated. Of course, not all features are reproduced by this model Hamiltonian throughout a small cubic region to which the model is restricted but it could serve as a useful tool for generating qualitative results to get a better understanding of this growing class of topological semimetals. For the nodal line, protected by inversion, time-reversal and spin rotation $SU(2)$ symmetries, the symmetry group Z_2 is the topological classification of the wave functions on the ring/sphere.¹⁸ Therefore, a nodal ring is characterized by two independent Z_2 indices, denoted by ζ_1 and ζ_2 , defined on a ring that links with the line and on a sphere that encloses the whole line. According to Ref. [18], all topological nodal rings, protected by this symmetry group with respect to an arbitrarily small perturbation, are characterized by $\zeta_1 = 1$. For NLSM with $\zeta_1 = 1$ and $\zeta_2 = 0$, our toy model Hamiltonian is given by¹⁸

$$\hat{H} = (\alpha - k^2)\hat{\sigma}_z + k_z\hat{\sigma}_x, \quad (1)$$

where energy is measured in units of $\hbar v_F k_c$ and the wave vector $\mathbf{k} = (k_x, k_y, k_z)$ is measured in units of k_c with the velocity $v_F \sim 1.5 \times 10^5$ m/s and k_c is the wave vector corresponds to momentum cut-off. Also, the energy is scaled with respect to $\hbar v_F k_c$, all wave vectors are scaled with respect to k_c and $-1 \leq k_i \leq 1$ with $i = x, y, z$ in order to ensure that the model is restricted near the O point. For convenience, we refer to this region as the cubic region. We have $\hat{\sigma}_x, \hat{\sigma}_z$ representing Pauli matrices. The quantity α is an adjustable parameter which can be employed to vary the energy gap around the O point for which the energy bands are given by

$$\epsilon_s(\mathbf{k}) = s\sqrt{k_z^2 + (\alpha - k^2)^2}. \quad (2)$$

These bands touch at $\mathbf{k} = 0$ when $\alpha = 0$. If $\alpha > 0$, the two subbands cross each other near the O point on the (k_x, k_y) plane for fixed $k_z = 0$, describing a nodal circle of radius $\sqrt{\alpha}$ which shrinks to a point at $\mathbf{k} = 0$ as α is decreased to zero and the nodal circle vanishes when $\alpha < 0$. In Fig. 1, we plot the energy bands in the small cubic region along lines joining given points, corresponding to $\alpha = 0$ and $\alpha = 0.5$. These two contrasting cases demonstrate how the band gap near O may be tuned by varying this parameter which may be manipulated as a function of strain. There are several mechanisms which one may use to engineer and tune the band structure. These include the interactions with substrates³⁸, strain³⁹⁻⁴¹, and time-dependent electromagnetic fields^{42,43}. It is clear from these results that the band structure is modified by finite α throughout the cubic region. Figure 1(b) shows that the bulk band gap closes at an even number of discrete points near the O point. These special gap closing points in the cubic region are protected by crystalline symmetry and play a role in the behavior of Weyl semimetals.⁴⁴ The detailed analysis of the topology of NLSMs, corresponding to the Hamiltonian in Eq. (1), is provided in Ref. [18]. This modification of the band structure has significant effects on the physical properties we calculate in this paper and may also affect the thermoelectric and Boltzmann transport as well as the plasmon excitations. In our model Hamiltonian, the gap is controlled by a parameter α as shown in Eq. (1) in the manuscript.

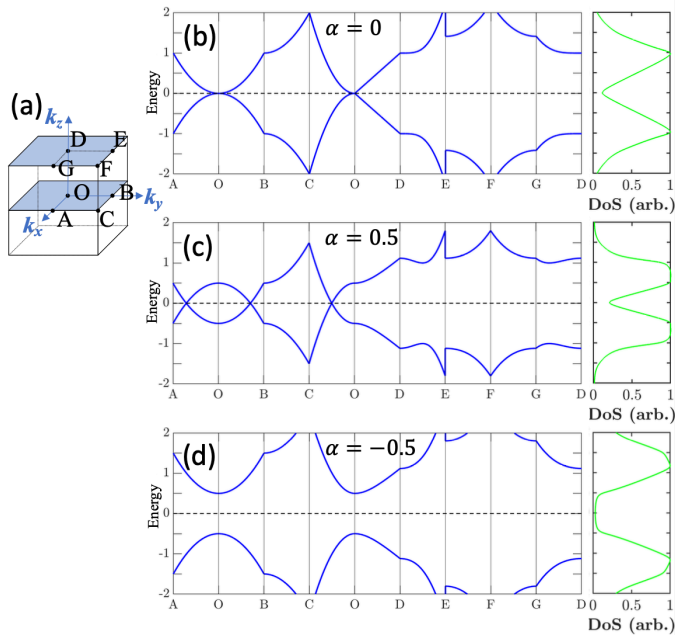


FIG. 1: (Color online) (a) shows the cubic region with some chosen symmetry points for the bulk NLSM. Bulk band structures between these symmetry points (left) and corresponding density-of-states (right) for (b) $\alpha = 0$, (c) $\alpha = 0.5$ and (d) $\alpha = -0.5$.

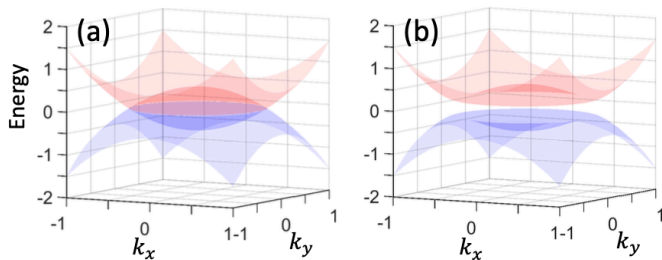


FIG. 2: (Color online) The 3D contour bands at low energy on the selected (k_x, k_y) plane for (a) $k_z = 0$ and (b) $k_z = 0.2$ at $\alpha = 0.5$. The pink curve corresponds to the conduction band ($s = +$) and the blue curve corresponds to the valence band ($s = -$)

The normalized eigenvectors φ_s (for $s = \pm$) of the Hamiltonian (1) are $\varphi_s^T(\mathbf{k}) = (\beta_s(\mathbf{k}), \eta_s(\mathbf{k})) \frac{e^{i\mathbf{k}\cdot\mathbf{r}}}{\sqrt{\mathcal{V}}}$, where \mathcal{V} is a normalization volume and β_s and η_s are given by $\beta_s^2(\mathbf{k}) = \frac{k_z^2}{k_z^2 + (k^2 - \alpha + s\sqrt{(k^2 - \alpha)^2 + k_z^2})^2}$ and $\eta_s^2(\mathbf{k}) = \frac{(k^2 - \alpha + s\sqrt{(k^2 - \alpha)^2 + k_z^2})^2}{k_z^2 + (k^2 - \alpha + s\sqrt{(k^2 - \alpha)^2 + k_z^2})^2}$ with $\beta_s^2 + \eta_s^2 = 1$.

Figure 1 shows the low-energy bands of the bulk NLSM along the line joining the symmetry points in the cubic region are anisotropic along the three perpendicular axes. When we go from O to A and B , the energy bands are symmetric but it is not so along the OD axis. For $\alpha = 0$, the two subbands touch at O making a flat dispersionless band in a small region around it. It is clearly seen that the dispersion around O is not linear like that for Dirac or Weyl semimetal. Therefore, we should not expect Dirac or Weyl-like optical conductivity even though two bands just touch at a point when the value of α is set to zero. For the numerical calculations, we have considered only two low energy bands and hence the effect of higher energy bands is neglected. The density-of-states has peak values for some energy range. The conductivity is expected to be a minimum for energy greater than that range. The 3D contour bands at low energy on the k_x, k_y plane are either crossed or gapped depending on the value of k_z as shown in Fig. 2. When $k_z = 0$, two bands cross. However, they open a gap on another plane for $k_z = 0.2$. While integrating over the cubic region, the effects from both planes are included which leads to finite values for both interband and intraband conductivity even for pristine NLSM.

We now introduce the Green's function defined by $\hat{\mathcal{G}}^{-1}(z) = z\hat{I} - \hat{H}$ which in matrix form is written as

$$\hat{\mathcal{G}}(\omega, \mathbf{k}) = \frac{1}{\mathcal{D}(\omega, \mathbf{k})} \begin{pmatrix} \omega + (\alpha - k^2) & k_z \\ k_z & \omega - (\alpha - k^2) \end{pmatrix}, \quad (3)$$

with $\mathcal{D}(\omega, \mathbf{k}) \equiv \omega^2 - (\alpha - k^2)^2 - k_z^2 = (\omega - \epsilon_+(\mathbf{k}))(\omega - \epsilon_-(\mathbf{k}))$.

Now, the spectral function representation of the Green's function is for $i, j = 1, 2$

$$\mathcal{G}_{ij}(z) = \int_{-\infty}^{\infty} \frac{d\omega'}{2\pi} \frac{A_{ij}(\omega')}{z - \omega'}. \quad (4)$$

The elements for the spectral function defined by Eq. (4) are

$$\begin{aligned} A_{11}(\mathbf{k}, \omega) &= \frac{2\pi}{\epsilon_+ - \epsilon_-} \{(\epsilon_+ + (\alpha - k^2))\delta(\omega - \epsilon_+) - (\epsilon_- + (\alpha - k^2))\delta(\omega - \epsilon_-)\} \\ A_{22}(\mathbf{k}, \omega) &= \frac{2\pi}{\epsilon_+ - \epsilon_-} \{(\epsilon_+ - (\alpha - k^2))\delta(\omega - \epsilon_+) - (\epsilon_- - (\alpha - k^2))\delta(\omega - \epsilon_-)\} \\ A_{12}(\mathbf{k}, \omega) &= A_{21}(\mathbf{k}, \omega) = \frac{2\pi k_z}{\epsilon_+ - \epsilon_-} \{\delta(\omega - \epsilon_+) - \delta(\omega - \epsilon_-)\}. \end{aligned} \quad (5)$$

An example of computing the elements of spectral function from Eq. (4) is given in the Appendix A. We can write the real part of the optical conductivity tensor as a function of the frequency Ω , which denotes the frequency of the external time-dependent electromagnetic field resonantly driving the allowed transitions between energy states of the system. We have

$$\begin{aligned} \sigma_{\alpha\beta}(\Omega) &= \frac{N_f e^2}{2\Omega} \int_{-\infty}^{\infty} \frac{d\omega}{2\pi} [f(\omega - \mu) - f(\omega + \Omega - \mu)] \\ &\times \int \frac{d^3\mathbf{k}}{(2\pi)^3} Tr \left[\hat{v}_\alpha \hat{A}(\mathbf{k}, \omega + \Omega) \hat{v}_\beta \hat{A}(\mathbf{k}, \omega) \right], \end{aligned} \quad (6)$$

where N_f is a degeneracy factor for the spin, e is the elementary charge, $f(\omega)$ is the Fermi-Dirac distribution function, μ is the chemical potential and $\hbar\hat{v}_\alpha = \partial\hat{H}/\partial k_\alpha$ gives the velocity matrices \hat{v}_α . Also, α, β represent spatial coordinates x, y, z . For the longitudinal in-plane conductivity, we have $\hat{v}_x = -2k_x\hat{\sigma}_z$, $\hat{v}_y = -2k_y\hat{\sigma}_z$ and $\hat{v}_z = -2k_z\hat{\sigma}_z + \hat{\sigma}_x$. For temperature $T = 0$ K, the Fermi function acts as a step function so the integration limit changes to $|\mu| - \Omega$ to $|\mu|$. In order to simplify the expressions, we chose E_k to represent the magnitude of energy eigenvalue. Hence, we replaced $\epsilon_+(\mathbf{k}) = E_k$ and $\epsilon_-(\mathbf{k}) = -E_k$. Putting these results together, we conclude that the longitudinal conductivity $\sigma_{xx}(\Omega)$, $\sigma_{yy}(\Omega)$ and $\sigma_{zz}(\Omega)$ are

$$\begin{aligned} \sigma_{xx}(\Omega) &= \frac{N_f e^2}{2\hbar\Omega\pi^2} \int_{|\mu|-\Omega}^{|\mu|} d\omega \int d^3\mathbf{k} k_x^2 \\ &\times \left\{ \left[1 - \frac{k_z^2}{E_k^2} \right] [\delta(\omega + \Omega - E_k)\delta(\omega - E_k) + \delta(\omega + \Omega + E_k)\delta(\omega + E_k)] \right. \\ &\left. + \frac{k_z^2}{E_k^2} [\delta(\omega + \Omega - E_k)\delta(\omega + E_k) + \delta(\omega + \Omega + E_k)\delta(\omega - E_k)] \right\} \end{aligned} \quad (7)$$

$$\begin{aligned} \sigma_{yy}(\Omega) &= \frac{N_f e^2}{2\hbar\Omega\pi^2} \int_{|\mu|-\Omega}^{|\mu|} d\omega \int d^3\mathbf{k} k_y^2 \\ &\times \left\{ \left[1 - \frac{k_z^2}{E_k^2} \right] [\delta(\omega + \Omega - E_k)\delta(\omega - E_k) + \delta(\omega + \Omega + E_k)\delta(\omega + E_k)] \right. \\ &\left. + \frac{k_z^2}{E_k^2} [\delta(\omega + \Omega - E_k)\delta(\omega + E_k) + \delta(\omega + \Omega + E_k)\delta(\omega - E_k)] \right\} \end{aligned} \quad (8)$$

$$\begin{aligned}
\sigma_{zz}(\Omega) = & \frac{N_f e^2}{8\hbar\Omega\pi^2} \int_{|\mu|-\Omega}^{|\mu|} d\omega \int d^3\mathbf{k} \left\{ \left[4k_z^2 \left(1 - \frac{k_z^2}{E_k^2} - \frac{(\alpha - k^2)}{E_k^2} \right) \right. \right. \\
& + \frac{k_z^2}{E_k^2} \left. \left[\delta(\omega + \Omega - E_k) \delta(\omega - E_k) + \delta(\omega + \Omega + E_k) \delta(\omega + E_k) \right] \right. \\
& + \left. \left[4 \frac{k_z^2}{E_k^2} \left[k_z^2 + (\alpha - k^2) \right] + \left(1 - \frac{k_z^2}{E_k^2} \right) \left[\delta(\omega + \Omega - E_k) \delta(\omega + E_k) \right. \right. \right. \\
& \left. \left. \left. + \delta(\omega + \Omega + E_k) \delta(\omega - E_k) \right] \right\} . \tag{9}
\end{aligned}$$

These terms give the intraband and interband contributions to the conductivity due to transitions within the conduction band and from transitions between the valence and conduction bands, respectively. The terms proportional to $[\delta(\omega + \Omega - E_k) \delta(\omega - E_k) + \delta(\omega + \Omega + E_k) \delta(\omega + E_k)]$ vanish when $\Omega > 0$ and give only the intraband conductivity. Similarly, the terms proportional to $[\delta(\omega + \Omega - E_k) \delta(\omega + E_k) + \delta(\omega + \Omega + E_k) \delta(\omega - E_k)]$ do not vanish for finite Ω and give interband conductivity. The significance of these contributions is determined by the level of doping, the frequency Ω and implicitly by α through the energy dispersion $\epsilon_s(\mathbf{k})$. The limit when $\Omega \rightarrow 0$ corresponds to the Drude conductivity.⁴⁵ We analyzed these intraband (Drude) conductivity using a Lorentzian expression for the δ function.

Similarly, the transverse component of the conductivities are

$$\sigma_{xy}(\Omega) = \frac{N_f e^2}{2\Omega} \int_{-\infty}^{\infty} \frac{d\omega}{2\pi} [f(\omega - \mu) - f(\omega + \Omega - \mu)] \int \frac{d^3\mathbf{k}}{(2\pi)^3} (4k_x k_y) \gamma(\mathbf{k}, \omega; \Omega). \tag{10}$$

$$\sigma_{yz}(\Omega) = \frac{N_f e^2}{2\hbar\Omega} \int_{-\infty}^{\infty} \frac{d\omega}{2\pi} [f(\omega - \mu) - f(\omega + \Omega - \mu)] \int \frac{d^3\mathbf{k}}{(2\pi)^3} \{-2k_y \kappa(\mathbf{k}, \omega; \Omega) + 4k_y k_z \gamma(\mathbf{k}, \omega; \Omega)\} \tag{11}$$

$$\sigma_{xz}(\Omega) = \frac{N_f e^2}{2\hbar\Omega} \int_{-\infty}^{\infty} \frac{d\omega}{2\pi} [f(\omega - \mu) - f(\omega + \Omega - \mu)] \int \frac{d^3\mathbf{k}}{(2\pi)^3} \{-2k_x \kappa(\mathbf{k}, \omega; \Omega) + 4k_x k_z \gamma(\mathbf{k}, \omega; \Omega)\} . \tag{12}$$

Clearly, the integrands in Eq. (10), (11) and (12) with values of γ and κ from (B1) and (B2), all are an odd function of k_x and k_y thereby making $\sigma_{xy}(\Omega)$, $\sigma_{yz}(\Omega)$ and $\sigma_{xz}(\Omega)$ zero.

The expressions for the conductivity $\sigma_{xx}(\Omega)$ and $\sigma_{yy}(\Omega)$ are symmetric. Thus, we employ Eq. (7) and (9) in the following section to carry out our numerical calculations for the longitudinal optical conductivity. These results exhibit the anisotropy of this NLSM system and demonstrate their dependence on the parameter α and the chemical potential μ as the frequency is varied.

III. RESULTS AND DISCUSSION FOR THE LONGITUDINAL CONDUCTIVITY

We now examine in detail with our numerical solutions the real part of the longitudinal optical conductivity of an anisotropic NLSM along the radial x , y and axial z directions. For the calculations, we have used $N_f = 2$ corresponds to the spin degeneracy, the small momentum cutoff with $-1 \leq k_{x,y,z} \leq 1$ to lie within the cubic region and a Lorentzian representation for the Dirac delta function, i.e., $\delta(x) \rightarrow \frac{\eta}{\pi} \frac{1}{\eta^2 + x^2}$ with a broadening of $\eta = 0.05$. This broadening takes into account the scattering due to non-magnetic impurities and lattice defects. The broadening is manifest in the optical conductivity as an effective transport scattering rate of $\frac{1}{\tau} = 2\eta$. It is convenient to scale the conductivity by $\sigma_0 = e^2/4\hbar$ and we set $\hbar = 1$ in the above Kubo formula. The finite temperature responses are also analyzed using the Fermi-Dirac distribution function at temperature T .

The transverse optical conductivity vanishes because of rotational symmetry of the NLSM. The longitudinal conductivities along different directions are obtained accordingly with the band structure and density-of-states plots. The anisotropic optical responses of the NLSM are depicted in Fig. 3 considering separately two chosen values of μ . The

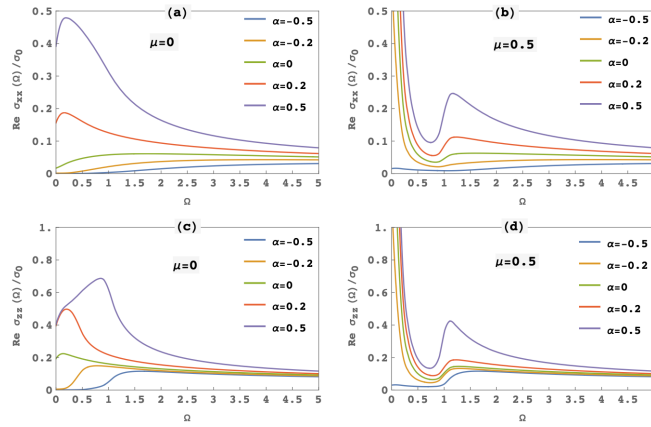


FIG. 3: (Color online) Real part of the longitudinal optical conductivity at $T = 0$ K measured along the x and z directions in the top to bottom panels, respectively, when (a) and (c) for $\mu = 0$ and (b) and (d) for $\mu = 0.5$ for five chosen values of the tuning parameter α . As the value of α is decreased, the conductivity becomes flatter and less dependent on frequency. The given NLSM admits similar responses along x and y and slightly different response along the z direction both quantitatively and qualitatively. μ , α and Ω are scaled with respect to energy unit $\hbar v_F k_c$.

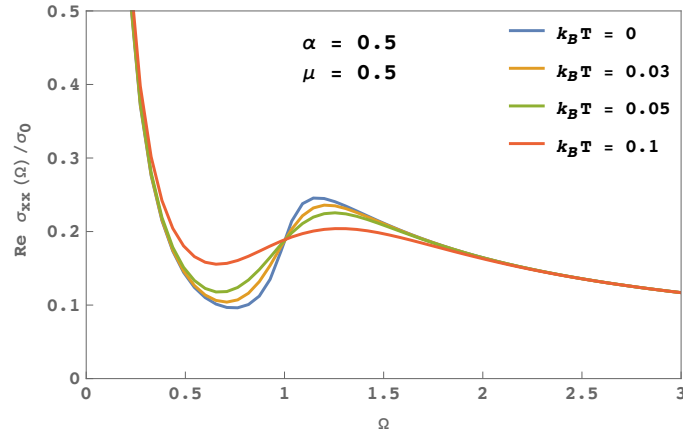


FIG. 4: (Color online) The real part of the optical conductivity along the x -axis is plotted as a function of photon energy Ω for fixed chemical potential $\mu = 0.5$ and adjustable parameter $\alpha = 0.5$. The different curves corresponds to the various scaled temperature ($k_B T = 0, 0.03, 0.05, 0.1$) as indicated. Conductivity is normalized with σ_0 and μ , α , Ω and $k_B T$ are scaled in terms of energy unit $\hbar v_F k_c$. When the temperature is increased from 0 K, the response slightly reduces and the curve becomes more flat at low frequency region.

conductivities along x and y are similar. However, along the z direction, the interband contribution for both pristine ($\mu = 0$) and the doped ($\mu = 0.5$) NLSM has greater value. The delta peak near Ω equal to zero called intraband or Drude conductivity, is due to the transition of electrons within the conduction band which we have numerically calculated using the Lorentzian representation for the Dirac delta function in the expression. The non-zero value of optical conductivity even at zero frequency is due to the topologically protected gapless states on the nodal line. This feature of the optical frequency makes the topological NLSM different from narrow band gap semiconductor, where the optical conductivity is typically zero at zero frequency. These properties indicate possible applications involving microelectronics technologies. These could include integrated circuits, ultrafast modulators and high performance transistors, as well as the development of self-detection of current-surge-induced overheating in electronic devices.

In the case of finite μ , we have zero conductivity for frequency less than 2μ and a finite jump for frequency greater than 2μ which reveals that the conductivity is due to interband transitions and that transitions obey the Pauli exclusion principle. For photon energy greater than 2μ , the conductivity reaches a maximum value and then is decreased to a minimum saturated value. The peak of the curve depends significantly on the tunable parameter α as well as the chemical potential μ . The conductivity becomes flat and the strength is reduced when α continuously goes from finite positive value to negative value. Specifically, the intensity of optical conductivity is reduced when a sizeable

gap is opened by tuning the value of α . On the other hand, the spectral weight of the conductivity tensor seems to be inversely dependent on the chemical potential. As we increase the chemical potential from zero, the intraband conductivity near zero frequency sharply rises but the strength of the optical absorption is reduced. Therefore for the further increase in the value of μ , the absorption peak move to the higher frequency region and the height also reduces. It means the electrons deep inside the valance band excite to the conduction band which require more photons with enough energy. Carbotte and Mukherjee^{6,7} have reported the flat conductivity in NLSM with notable finite height. However, our results are similar to that for ZrSiS.⁹ In fact, Habe and Koshino demonstrated that the optical conductivity of a NLSM such as ZrSiS takes the peak value and then sharply falls to a flat plateau region and again rises up in the high frequency region. Throughout these calculations, we have considered a toy-model Hamiltonian with only two subbands and small momentum cutoff. Consequently, these results are applicable for small values of chemical potential and for low frequency. For large values of chemical potential and for higher frequency range, the contribution from other subbands to the conductivity may be significant and the conductivity may again increase. The effect due to finite temperature manifests itself through similar qualitative behavior. Figure 4 demonstrates that when the temperature is increased from 0 K, the magnitude and the slope of the interband optical conductivity curve is slightly reduced. This is because the thermally excited electrons and holes are perturbed by the optical transitions from the valance to the conduction band in the low-frequency regime. When the temperature is further increased from room temperature, the curve becomes more flat. This means that the effect due to temperature is not as significant as it is in the low-temperature regime. We generalized this finite temperature response for the 4×4 matrix model Hamiltonian which we describe below.

IV. DENSITY-OF-STATES

For the density-of-states, we have

$$N(\omega) = N_f \int \frac{d^3\mathbf{k}}{(2\pi)^3} \sum_{s=\pm} \delta(\omega - \epsilon_s(\mathbf{k})) \quad (13)$$

for which we again employ a Lorentzian representation for the delta function. The effects due to the gaps between the energy subbands that are generated by the positive parameter α are clearly reflected in the density-of-states. The presented density-of-states in Fig. 5 are for three values of $\alpha = 0, 0.5$ and 1.0

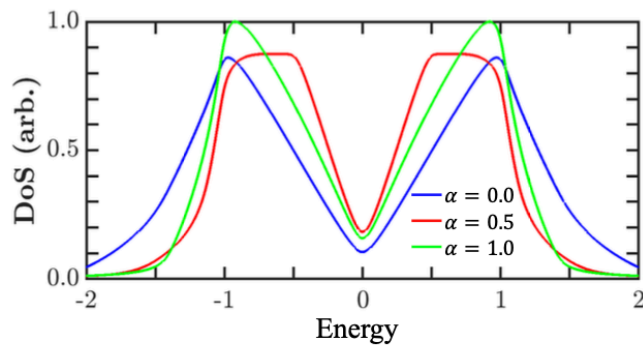


FIG. 5: (Color online) Density-of-states for chosen values of α . Energy and α are scaled with respect to $\hbar v_F k_c$.

V. ANOTHER EXAMPLE OF A NODAL-LINE SEMIMETAL

An effective Hamiltonian for electrons in nodal-line semimetals with Z_2 indices $\zeta_1 = 1$ and $\zeta_2 = 1$ is given by¹⁸

$$\hat{H}(\mathbf{k}) = k_x s_x \otimes I + k_y s_y \otimes \tau_y + k_z s_z \otimes I + \alpha \tau_x \otimes s_x, \quad (14)$$

where \otimes is the Kronecker product of two matrices. For the model Hamiltonian (14), by varying the value of α from positive to negative, the nodal line on the $k_x - k_y$ plane of radius $|\alpha|$, first shrinks to a point, then evolves into a

“line” again. This means that one cannot open a gap between the valance and conduction band just by varying the parameter α . The shape and extent of the nodal line change symmetrically for positive and negative α . The detailed analysis of topology of NLSMs is provided in Ref. [18]. The Hamiltonian $\hat{H}(\mathbf{k})$ in Eq. (14) reads in matrix form as

$$\hat{H}(\mathbf{k}) = \begin{pmatrix} k_z & 0 & k_x & (\alpha - k_y) \\ 0 & k_z & (\alpha + k_y) & k_x \\ k_x & (\alpha + k_y) & -k_z & 0 \\ (\alpha - k_y) & k_x & 0 & -k_z \end{pmatrix}. \quad (15)$$

The eigenvalues $\epsilon_{s,s'}(\mathbf{k})$ of $\hat{H}(\mathbf{k})$ from Eq. (15) are

$$\epsilon_{s,s'}(\mathbf{k}) = s \sqrt{k_z^2 + \left(\sqrt{k_x^2 + k_y^2} + s'\alpha \right)^2}. \quad (16)$$

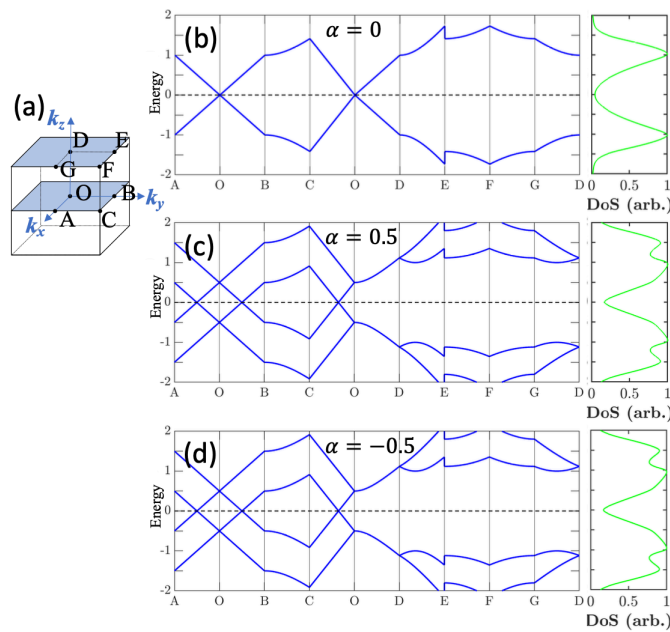


FIG. 6: (Color online) (a) Low-energy subbands of bulk NLSM described by the Hamiltonian in Eq. (14). The results are within a cubic region with indicated symmetry points. Bulk bands along lines joining the given symmetry points (left) and corresponding density-of-states (right) for (b) $\alpha = 0$, (c) $\alpha = 0.5$ and (d) $\alpha = -0.5$. The bands and density-of-states are symmetric for $\alpha = 0.5$ and $\alpha = -0.5$.

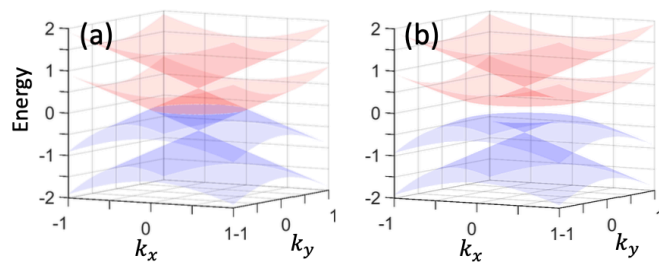


FIG. 7: (Color online) The 3D contour bands at low energy on the selected (k_x, k_y) planes for (d) $k_z = 0$ and (e) $k_z = 0.2$ at $\alpha = 0.5$. The pink curve corresponds to the conduction band ($s = +$) and the blue curve corresponds to the valance band ($s = -$)

Also, we have determined the eigenvectors for this case but the expressions are long and unwieldy and not needed for calculating the optical conductivity. We will need these for determining the plasmon dispersion. For calculating $\sigma_{\alpha\beta}(\Omega)$, we employ

$$\hat{v}_x = \begin{pmatrix} 0 & 0 & 1 & 0 \\ 0 & 0 & 0 & 1 \\ 1 & 0 & 0 & 0 \\ 0 & 1 & 0 & 0 \end{pmatrix}, \quad \hat{v}_y = \begin{pmatrix} 0 & 0 & 0 & -1 \\ 0 & 0 & 1 & 0 \\ 0 & 1 & 0 & 0 \\ -1 & 0 & 0 & 0 \end{pmatrix}, \quad \hat{v}_z = \begin{pmatrix} 1 & 0 & 0 & 0 \\ 0 & 1 & 0 & 0 \\ 0 & 0 & -1 & 0 \\ 0 & 0 & 0 & -1 \end{pmatrix} \quad (17)$$

$$\begin{aligned} \epsilon_1 &= \epsilon_{++} = \sqrt{k_z^2 + (\sqrt{k_x^2 + k_y^2} + \alpha)^2} \\ \epsilon_2 &= \epsilon_{+-} = \sqrt{k_z^2 + (\sqrt{k_x^2 + k_y^2} - \alpha)^2} \\ \epsilon_{-+} &= -\epsilon_1 \text{ and } \epsilon_{--} = -\epsilon_2 \end{aligned} \quad (18)$$

In this case, the Green's function and the spectral function have the matrix elements in the form

$$\hat{G}_{11}(\omega) = \frac{1}{\mathcal{D}_2(\omega)} \{-\alpha^2 k_z - \omega\alpha^2 - 2\omega k_y k_z - 2\omega\alpha k_y - k_x^2 k_z - \omega k_x^2 - k_y^2 k_z - \omega k_y^2 - k_z^3 - \omega k_z^2 + \omega^2 k_z + \omega^3\} \quad (19)$$

And

$$A_{11}(\omega) = \frac{\pi}{4\alpha} \frac{\omega + k_z}{\sqrt{k_x^2 + k_y^2}} (\omega^2 - k_z^2 - k_x^2 - k_y^2 - \alpha^2 - 2\alpha k_y) \left\{ \frac{1}{\epsilon_1} (\delta(\omega - \epsilon_1) - \delta(\omega + \epsilon_1)) - \frac{1}{\epsilon_2} (\delta(\omega - \epsilon_2) - \delta(\omega + \epsilon_2)) \right\} \quad (20)$$

The other elements have the similar expressions. The function $\mathcal{D}_2(\omega) = (\omega - \epsilon_{+,+})(\omega - \epsilon_{+,-})(\omega - \epsilon_{-,+})(\omega - \epsilon_{-,-})$ where the eigenvalues are given in Eq. (16). Using the Kubo formula Eq. (6), the real part of longitudinal optical conductivity is obtained as

$$\sigma_{xx}(\Omega) = \frac{N_f e^2}{2\hbar\Omega(2\pi)^4} \int_{|\mu|-\Omega}^{|\mu|} d\omega \int d^3\mathbf{k} \Delta(\mathbf{k}, \omega; \Omega) \quad (21)$$

$$\sigma_{yy}(\Omega) = \frac{N_f e^2}{2\hbar\Omega(2\pi)^4} \int_{|\mu|-\Omega}^{|\mu|} d\omega \int d^3\mathbf{k} \Sigma(\mathbf{k}, \omega; \Omega) \quad (22)$$

$$\sigma_{zz}(\Omega) = \frac{N_f e^2}{2\hbar\Omega(2\pi)^4} \int_{|\mu|-\Omega}^{|\mu|} d\omega \int d^3\mathbf{k} \Lambda(\mathbf{k}, \omega; \Omega) \quad (23)$$

where, the expressions for $\Delta(\mathbf{k}, \omega; \Omega)$, $\Sigma(\mathbf{k}, \omega; \Omega)$ and $\Lambda(\mathbf{k}, \omega; \Omega)$ are given in the Appendix C.

Needless to say, a single model Hamiltonian cannot explain all types of semimetals. Different model Hamiltonians can be used to understand various materials of NLSM groups. This is exemplified in the work of these two references [10] and [17]. It depends on the shape, size and nature of the nodal line. Since the radius of the nodal ring can vary, depending on the strength of the tuning parameter, we have investigated the optical responses of such NLSM whose nodal ring does not shrink to a point and is gapped by tuning the parameter α . We have characterized the optical conductivity considering the effective Hamiltonian in Eq. (14) which has four eigenvalues corresponds to four subbands in the low-energy cubic region. Two valence bands and two conduction bands are clearly outlined in the band structure plot in Fig. 6. When the value of α is set to zero, only two subbands are present within this cubic region and the subbands are symmetric along three axes and are linearly dispersed around the O point as that for Dirac or Weyl semimetals. However, for finite value of α , two subbands are present within the this cubic region and they are not symmetrically dispersive as we go from O to A or B and O to D . We are more focused on the results for

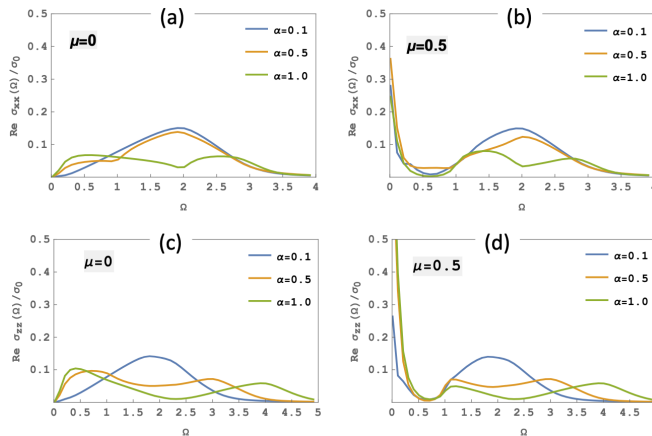


FIG. 8: (Color online) Real part of the longitudinal optical conductivity of nodal-line semimetal described by the model Hamiltonian in Eq. (14) at $T=0$ K, (a) and (b) along the x direction and (c) and (d) along the z direction when (a) and (c) for $\mu = 0$ and (b) and (d) for $\mu = 0.5$ with chosen values of the tuning parameter α . μ , α and Ω are scaled with respect to energy unit $\hbar v_F k_c$.

finite α . The conduction and valence bands are gapped in parallel planes for k_z not equal to zero as shown in Fig. 7. The density-of-states also has two peaks and has finite value for larger range of energy than the previous model.

The optical conductivities presented in Fig. 8 are in accordance with the band structure and density-of-states for the Hamiltonian in Eq. (14). Various types of intraband and interband transition channels are allowed. During the process of our calculations, we have set $N_f = 2$ to include the spin degeneracy of the bands. For charge neutral pristine NLSM, zero conductivity at $\Omega \rightarrow 0$ reveals that there are no allowed transitions within the subbands. Therefore, the total conductivity for $\mu = 0$ is the contribution from interband transitions. As the Fermi level rises up to a positive value, intraband conductivity contributions are achieved and delta peaks appear around Ω tending to zero. Unlike the previous model Hamiltonian, the conductivity is inversely proportional to α . As the value of α is increased from 0.1, the height of the single peak is reduced and is split into two reduced peaks for α around 1.0. Eventually, all curves saturates to a minimum value. The nature of the curves is slightly different in the upper (σ_{xx}) and lower (σ_{zz}) plots. For larger values of α , the curves are flatter along z than that along x which reveals the anisotropy of the conductivity.

VI. THERMAL PROPERTIES

We employ the Wilson-Sondheim formula^{46,47} for the grand thermodynamic potential of a Fermi-Dirac gas of noninteracting electrons. We have per unit volume

$$\Omega(T, \mu) = -k_B T \frac{1}{V} \sum_{\mathbf{k}, s} \ln \left[1 + e^{-\beta(E_{\mathbf{k}, s} - \mu)} \right] \quad (24)$$

where V is a normalization volume and $E_{\mathbf{k}, s}$ is energy eigenvalue given in Eq. (2). The calculated grand potential can be further used to calculate several thermodynamic quantities for various temperatures and densities. It is worthy of note that $\Omega(T, \mu)$ may also be expressed in terms of the inverse Laplace transform of the partition function^{46,47} $Z(s) = \sum_{\{\omega\}} e^{-s\omega}$, where the sum is carried out over the eigenstates, with an appropriate cut-off for the wave vector. The specific heat capacity is

$$\begin{aligned} C_V &= T \frac{\partial S}{\partial T} = -\beta \frac{\partial S}{\partial \beta} \\ &= \frac{k_B \beta^2}{2} \frac{1}{V} \sum_{\mathbf{k}, s} \frac{(E_{\mathbf{k}, s} - \mu)^2}{\cosh^2(\beta(E_{\mathbf{k}, s} - \mu))/2} \end{aligned} \quad (25)$$

which follows from the entropy

$$\begin{aligned}
 S &= k_B \beta^2 \frac{\partial \Omega}{\partial \beta} \\
 &= k_B \frac{1}{V} \sum_{\mathbf{k},s} \ln \left[1 + e^{-\beta(E_{\mathbf{k},s} - \mu)} \right] + k_B \beta \frac{1}{V} \sum_{\mathbf{k},s} (E_{\mathbf{k},s} - \mu) \left\{ 1 - \tanh \left(\frac{\beta(E_{\mathbf{k},s} - \mu)}{2} \right) \right\}
 \end{aligned} \tag{26}$$

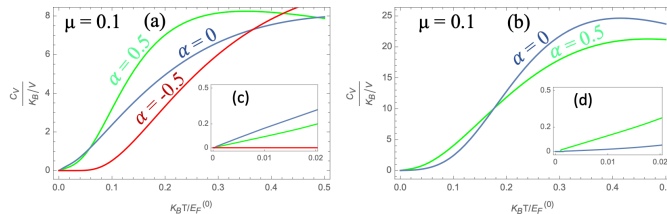


FIG. 9: (Color online) Temperature variation of specific heat capacity at constant volume (a) for the model Hamiltonian in Eq. (1) and (b) for the model Hamiltonian in Eq. (14) for $\mu = 0.1$. (c) and (d) are the low-temperature portions of (a) and (b) respectively. The different curves are for different values of the tuning parameter α as indicated. C_V is normalized to constant value K_B/V and $K_B T$ is normalized to energy $E_F^{(0)} = \hbar v_f k_c$.

Numerical results for the specific heat capacity are presented in Fig. 9. Plots (a) and (b) are for the two model Hamiltonians considered in Eqs. (1) and (14). For Fig. 9 (b), the energy is given by Eq. (16) and the summation is taken over all subbands s and s' . We have found that the heat capacity is low at very low temperatures. As the temperature is increased, it rises linearly with temperature and attains a saturated value following the Debye/Einstein law. However, the saturation temperature and low-temperature response are strongly dependent on the tuning parameter α . The heat capacity variation with temperature around room temperature is shown in the zoom-in part of each plot. It shows that, the heat capacity with tuning parameter α in the low temperature region is different for the two model Hamiltonians considered. For instance, in Fig. 9(c), the curve for $\alpha = 0$ has higher slope than that for $\alpha = 0.5$ and for $\alpha = -0.5$ it is zero. On the other hand, in Fig. 9(d), the curve for $\alpha = 0$ has lower slope than that for $\alpha = \pm 0.5$. It signifies that one can vary the specific heat capacity by tuning the gap in the NLSM.

VII. SUMMARY AND CONCLUSIONS

In conclusion, we have theoretically investigated the linear responses of nodal-line semimetal using two simple models in conjunction with the Kubo formula for the optical conductivity as well as their heat capacity when in thermal equilibrium. We have derived closed-form expressions for the longitudinal and transverse components of the dynamical optical conductivity for both of these simple models whose energy subband structures are anisotropic in \mathbf{k} space. It has been found that NLSM presents different thermal behavior depending on the gap in the band structure. We may also employ the grand potential to calculate other thermodynamic properties such as compressibility, expansion coefficient and sound velocity. These model Hamiltonians are simple yet their energy subband structures bear similarities to calculated results using the tight-binding model near the Fermi level of a nodal-line semimetal under strain. This effect due to strain is introduced through a parameter α in the model Hamiltonian, thereby making these simple models useful for predictions for the NLSM using this approach. This is bolstered not only by similarities in the band structure but the overall qualitative behavior of the conductivity when compared with a material such as ZrSiS. We have presented results for the optical conductivity as a function of frequency at both zero and finite temperature. We analyzed the results considering the effect of varying the parameter α for two different models of nodal-line semimetal and chemical potential. We have plotted the subband structure along lines joining given symmetry points in a low-energy cubic region in a chosen (k_x, k_y) plane. We emphasize that the continuum model Hamiltonian yields energy bands near the O point in the (k_x, k_y) plane but these results could be quite different in parallel planes. As we go from some positive value of α to zero, the crossing of the valence and conduction bands changes from nodal ring to 3D point node. However, for negative value of α , the dispersion is different for the two models. For the 2×2 matrix model Hamiltonian, the valence and conduction bands separate and a gap opens near the O point while for the 4×4 matrix model Hamiltonian they again cross, making a nodal ring. This means that one cannot tune one Hamiltonian to the

other without closing the gap. Therefore, these two model Hamiltonians are not topologically equivalent and hence the drastic difference in the optical conductivity of these two models signifies that the optical responses of such NLSM are sensitive to topology. Additionally, we do not expect similar features in a trivial semiconductor with tunable band gap because the band structure is different from the ones obtained for the two model Hamiltonians for NLSM, presented in this paper. The specific heat capacity is also different for the two models. Furthermore, the results we obtained for the dynamical optical conductivity are in qualitative agreement with those reported using realistic band structures. In the Table 1, we have listed the references in which the optical response of different NLSM materials has been studied experimentally and theoretically.

Table 1: The following references studied the optical conductivity of NLSM materials experimentally and theoretically.

Reference	Case study
[6]	Cd ₃ As ₂ , TaAs, Eu ₂ In ₂ O ₇ , ZnTe ₅
[7]	nodal loop semimetals
[8]	body-centered orthorhombic C ₁₆ , CaP ₃ , Ca ₃ P ₂
[9]	ZrSiS, ZrSiSe, ZrSiTe, HfSiS
[11]	tilted NLSM
[12]	ZrSiS
[13]	YbMnSb ₂
[14]	ZrSiS, ZrSiSe, ZrSiTe, ZrGeS, ZrGeTe
[15]	ZrGeS, ZrGeSe
[16]	ZrSiS

The transverse conductivity vanishes due to rotational symmetry along the nodal ring of the semimetal. Regarding the longitudinal component, for charge neutral NLSM, the interband conductivity is significant near zero frequency. However, for doped NLSM with chemical potential μ , the interband conductivity rises to the peak value at $\Omega = 2\mu$ and is then decreased. For frequency less than 2μ , Pauli blocking makes electrons unable to make transitions in the valence and conduction bands. At higher photon energies, the transition saturates at its minimum value. This can be explained as a consequence of the low-energy cut-off and the resulting limits on the wave vector $\mathbf{k} = (k_x, k_y, k_z)$ scaled by k_c which is restricted to $|k_i| \leq 1$ ($i = x, y, z$). The Hamiltonian \hat{H} , Ω , α and μ are all scaled in terms of the energy unit $\hbar v_F k_c$. Therefore, the conductivity of NLSM depends on v_F and k_c . The height and width of the peak depend principally on the tuning parameter (α). For $\alpha = 0$, the curve is almost flat at very small transition. At $\alpha = 0$, the bands touch at a point but the quadratic dispersion near O is not linear like Dirac or Weyl. Therefore, the conductivity is not flat like that of 2D and 3D Dirac materials as explained in Refs. [6–8]. As we increase the value of α from 0 to larger values, the peak becomes sharper and sharper. In any event, they all converge to a minimum saturated value in the higher frequency region. This is also in agreement with density-of-states plots. The density-of-states has a peak at a certain energy and is zero over a range which could be adjusted by manipulating the value of α . The anisotropic dispersion relation along radial (k_x, k_y) and axial (k_z) directions results in their anisotropic conductivity along these directions. The conductivity along x and y are identical yet the conductivity along z deviates slightly both quantitatively and qualitatively. The anisotropic conductivities in Shahin's⁸ paper are explained as a consequence of an anisotropic Fermi surface for which they have considered a toroidal shape.

The nodal lines in these model Hamiltonians are protected by three symmetries such as inversion symmetry, time-reversal symmetry and spin rotation $SU(2)$ symmetry. Since the SOC has not been considered, these symmetries are preserved under the application of strain. When SOC is introduced, these symmetries can be broken leading to the splitting of the line node into point nodes. This splitting of the line node into point node may affect the band structure and the density of states. Moreover, it can enhance light-matter interactions and give rise to new optical transitions. Therefore, we can expect the different features like changes in strength, changes in anisotropy as well as the appearance or disappearance of peaks in the spectrum of optical conductivity. A detailed analysis of optical conductivity in the presence of SOC is interesting in its own right.

Although the model Hamiltonians used undoubtedly have limitations, we believe that our work serves to complement the existing literature with our reported results for optical conductivity as well as thermal heat capacity and their dependence on the gap, temperature and doping. This will serve to advance our knowledge beyond the already known results. Additionally, there are several applications of NLSMs. Topological nodal-line semimetals with many exotic physical properties are potential candidates for next-generation device applications. For example, the high

photosensitivity is of importance for the construction of ultrafast photodetectors. The spin-momentum locking of the surface states could be used for low-consumption spintronic devices and magnetic memory devices. The nodal lines of the semimetal can be used to create protected qubits for the development of topological quantum computing. In addition, many topological nodal-line semimetals have large thermoelectric responses, which can be utilized for high-efficiency energy converters or thermal detectors.

Acknowledgement(s)

G.G. would like to acknowledge the support from the Air Force Research Laboratory (AFRL) through Grant No. FA9453-21-1-0046. We would like to thank Dr. Po-Hsin Shih and Dr. Thi-Nga Do for helpful discussions and guidance on the numerical calculations and interpretation of the results.

Appendix A: Spectral function

We have from Eq. (4) and setting $i = j = 1$

$$G_{11}(z) = \int_{-\infty}^{\infty} \frac{d\omega' A_{11}(\omega')}{2\pi(z - \omega')}$$

Resolving the left-hand side of this equation into partial fractions, we obtain

$$\frac{1}{(\epsilon_+ - \epsilon_-)} \left[\frac{[\epsilon_+ + (\alpha - k^2)]}{(z - \epsilon_+)} - \frac{[\epsilon_- + (\alpha - k^2)]}{(z - \epsilon_-)} \right] = \int_{-\infty}^{\infty} \frac{d\omega' A_{11}(\omega')}{2\pi(z - \omega')}$$

Now, let us rewrite the left-hand side of this equation in integral form which is possible when δ functions are introduced. The result is

$$\frac{1}{(\epsilon_+ - \epsilon_-)} \int_{-\infty}^{\infty} \frac{d\omega'}{z - \omega'} \left[[\epsilon_+ + (\alpha - k^2)] \delta(\omega' - \epsilon_+) - [\epsilon_- + (\alpha - k^2)] \delta(\omega' - \epsilon_-) \right] = \int_{-\infty}^{\infty} \frac{d\omega' A_{11}(\omega')}{2\pi(z - \omega')} .$$

From this latter equation, we clearly identify the spectral weight $A_{11}(z)$ as

$$A_{11}(z) = \frac{2\pi}{(\epsilon_+ - \epsilon_-)} \left[[\epsilon_+ + (\alpha - k^2)] \delta(z - \epsilon_+) - [\epsilon_- + (\alpha - k^2)] \delta(z - \epsilon_-) \right] .$$

Appendix B: Conductivity I

The following are the expressions for $\gamma(\mathbf{k}, \omega; \Omega)$ and $\kappa(\mathbf{k}, \omega; \Omega)$ in Eq. (10), (11) and (12) .

$$\begin{aligned} \gamma(\mathbf{k}, \omega; \Omega) &\equiv 4\pi^2 \left\{ \left[1 - \frac{k_z^2}{E_k^2} \right] [\delta(\omega + \Omega - E_k) \delta(\omega - E_k) + \delta(\omega + \Omega + E_k) \delta(\omega + E_k)] \right. \\ &\quad \left. + \frac{k_z^2}{E_k^2} [\delta(\omega + \Omega - E_k) \delta(\omega + E_k) + \delta(\omega + \Omega + E_k) \delta(\omega - E_k)] \right\} , \end{aligned} \quad (\text{B1})$$

$$\begin{aligned} \kappa(\mathbf{k}, \omega; \Omega) &\equiv \frac{4\pi^2 k_z (\alpha - k^2)}{E_k^2} \left\{ \delta(\omega + \Omega - E_k) \delta(\omega - E_k) - \delta(\omega + \Omega + E_k) \delta(\omega - E_k) \right. \\ &\quad \left. - \delta(\omega + \Omega - E_k) \delta(\omega + E_k) + \delta(\omega + \Omega + E_k) \delta(\omega + E_k) \right\} \end{aligned} \quad (\text{B2})$$

Appendix C: Conductivity II

The expressions for $\Delta(\mathbf{k}, \omega; \Omega)$, $\Sigma(\mathbf{k}, \omega; \Omega)$ and $\Lambda(\mathbf{k}, \omega; \Omega)$ in Eq. (21), (22) and (23) are given by,

$$\begin{aligned} \Delta(\mathbf{k}, \omega; \Omega) &= A_{11}(\omega + \Omega) A_{33}(\omega) + A_{33}(\omega + \Omega) A_{11}(\omega) + A_{22}(\omega + \Omega) A_{44}(\omega) + A_{44}(\omega + \Omega) A_{22}(\omega) \\ &\quad + 2A_{12}(\omega + \Omega) A_{34}(\omega) + 2A_{34}(\omega + \Omega) A_{12}(\omega) + 2A_{14}(\omega + \Omega) A_{23}(\omega) + 2A_{23}(\omega + \Omega) A_{14}(\omega) \\ &\quad + 4A_{13}(\omega + \Omega) A_{13}(\omega) \end{aligned} \quad (\text{C1})$$

$$\begin{aligned}
\Sigma(\mathbf{k}, \omega; \Omega) = & -2A_{12}(\omega + \Omega) A_{34}(\omega) - 2A_{34}(\omega + \Omega) A_{12}(\omega) + A_{22}(\omega + \Omega) A_{33}(\omega) + A_{33}(\omega + \Omega) A_{22}(\omega) \\
& + 2A_{23}(\omega + \Omega) A_{23}(\omega) + 2A_{14}(\omega + \Omega) A_{14}(\omega) + A_{44}(\omega + \Omega) A_{11}(\omega) + A_{11}(\omega + \Omega) A_{44}(\omega) \\
& - 4A_{13}(\omega + \Omega) A_{13}(\omega)
\end{aligned} \tag{C2}$$

$$\begin{aligned}
\Lambda(\mathbf{k}, \omega; \Omega) = & A_{11}(\omega + \Omega) A_{11}(\omega) + A_{22}(\omega + \Omega) A_{22}(\omega) + A_{33}(\omega + \Omega) A_{33}(\omega) + A_{44}(\omega + \Omega) A_{44}(\omega) \\
& + 2A_{12}(\omega + \Omega) A_{12}(\omega) + 2A_{34}(\omega + \Omega) A_{34}(\omega) - 2A_{14}(\omega + \Omega) A_{14}(\omega) - 2A_{23}(\omega + \Omega) A_{23}(\omega) \\
& - 4A_{13}(\omega + \Omega) A_{13}(\omega)
\end{aligned} \tag{C3}$$

-
- ¹ Lukas Muechler, Andreas Topp, Raquel Queiroz, Maxim Krivenkov, Andrei Varykhalov, Jennifer Cano, Christian R. Ast, and Leslie M. Schoop, Modular Arithmetic with Nodal Lines: Drumhead Surface States in ZrSiTe, *Phys. Rev. X* **10**, 011026 (2020).
- ² Haiyang Pan, Bingbing Tong, Jihai Yu, Jue Wang, Dongzhi Fu, Shuai Zhang, Bin Wu, Xiangang Wan, Chi Zhang, Xuefeng Wang, and Fengqi Song, Three-Dimensional Anisotropic Magnetoresistance in the Dirac Node-Line Material ZrSiSe, *Scientific Reports*, DOI:10.1038/s41598-018-27148-z (2018).
- ³ Yinming Shao, A. N. Rudenko, Jin Hu, Zhiyuan Sun, Yanglin Zhu, Seongphill Moon, A. J. Millis, Shengjun Yuan, A. I. Lichtenstein, Dmitry Smirnov, Z. Q. Mao, M. I. Katsnelson, and D. N. Basov, Electronic correlations in nodal-line semimetals, *Nature Physics* **16**, 636 (2020).
- ⁴ S.-M. Huang, S.-Y. Xu, I. Belopolski, C.-C. Lee, G. Chang, B.K. Wang, N. Alidoust, G. Bian, M. Neupane, C. Zhang, et al. A Weyl Fermion semimetal with surface Fermi arcs in the transition metal mononictide TaAs class. *Nat. Commun.* **6**, 7373 (2014).
- ⁵ C. Fang, L. Lu, J. Liu and L. Fu. Topological semimetals with helicoid surface states. *Nat. Phys.* **12**, 936 (2016).
- ⁶ J P Carbotte, Optical Response of a Line Node Semimetal, *J. Phys. Condens. Matter* **29**, 045301 (2017).
- ⁷ S. P. Mukherjee and J. P. Carbotte, Transport and Optics at The Node in a Nodal Loop Semimetal, *Phys. Rev. B* **95**, 214203 (2017).
- ⁸ Shahin Barati and Saeed H. Abedinpour, Optical conductivity of three and two dimensional topological nodal line semimetals. *Physical Review B*. **96**. 10.1103/PhysRevB.96.155150 (2017).
- ⁹ Tetsuro Habe and Mikito Koshino, Dynamical Conductivity in the Topological Nodal-Line Semimetal ZrSiS, *Phys. Rev. B* **98**, 125201 (2018).
- ¹⁰ Michael Phillips and Vivek Aji, Tunable line node semimetals, *Phys. Rev. B* **90**, 115111 (2014).
- ¹¹ Chen Wang, Wen-Hui Xu, Chang-Yong Zhu, Jin-Na Chen, Yong-Long Zhou, Ming-Xun Deng, Hou-Jian Duan and Rui-Qiang Wang, Anomalous Hall Optical Conductivity in Tilted Topological Nodal-Line Semimetals, *Phys. Rev. B* **103**, 165104 (2021).
- ¹² W. Zhou, A. N. Rudenko, and S. Yuan, *Adv. Electron. Mater.* **6**, 1, 1900860 (2020).
- ¹³ Ziyang Qiu, Congcong Le, Zhiyu Liao, Bing Xu, Run Yang, Jiangping Hu, Yaomin Dai, and Xianggang Qiu, Observation of a topological nodal-line semimetal in YbMnSb₂ through optical Spectroscopy. *Phys. Rev. B* **100**, 125136 (2019).
- ¹⁴ J. Ebad-Allah, J. Fernandez Afonso, M. Krottenmuller, J. Hu, Y. L. Zhu, Z. Q. Mao, J. Kunes, and C. A. Kuntscher, Chemical pressure effect on the optical conductivity of the nodal-line semimetals ZrSiY(Y=S, Se, Te) and ZrGeY(Y=S, Te), *Phys. Rev. B* **99**, 125154 (2019).
- ¹⁵ J. Ebad-Allah, S. Rojewski, Y. Li. Zhu, Z. Q. Mao, and C. A. Kuntscher, In-plane and out-of-plane optical response of the nodal-line semimetals ZrGeS and ZrGeSe., *Phys. Rev. B* **106**, 075143 (2022).
- ¹⁶ J. Ebad-Allah, S. Rojewski, M. Vost, G. Eickerling, W. Scherer, E. Uykur, Raman Sankar, L. Varrassi, C. Franchini, K. -H. Ahn, J. Kunes, and C. A. Kuntscher, Pressure-Induced Excitations in the Out-of-Plane Optical Response of the Nodal-Line Semimetal ZrSiS. *Phys. Rev. Lett.* **127**, 076402 (2021).
- ¹⁷ Zhongbo Yan, Peng-Wei Huang, and Zhong Wang, Collective modes in nodal line semimetals, *Phys. Rev. B* **93**, 085138 (2016).
- ¹⁸ Chen Fang, Hongming Weng, Xi Dai, and Zhong Fang, Topological nodal line semimetals, *Chinese Phys. B* **25**, 117106 (2016).
- ¹⁹ E. J. Nicol and J. P. Carbotte. Optical conductivity of bilayer graphene with and without an asymmetry gap. *Phys. Rev. B* **77**, 155409 (2008).
- ²⁰ S.-Y. Xu, C. Liu, S. K. Kushwaha, R. Sankar, J. W. Krizan, I. Belopolski, M. Neupane, G. Bian, N. Alidoust, T.-R. Chang, H.-T. Jeng, C.-Y. Huang, W.-F. Tsai, H. Lin, P. P. Shibayev, F.-C. Chou, R. J. Cava, and M. Z. Hasan, Observation of Fermi Arc Surface States in a Topological Metal, *Science* **347**, 294 (2015).
- ²¹ K. Deng, G. Wan, P. Deng, K. Zhang, S. Ding, E. Wang, M. Yan, H. Huang, H. Zhang, Z. Xu, J. Denlinger, A. Fedorov, H. Yang, W. Duan, H. Yao, Y. Wu, S. Fan, H. Zhang, X. Chen, and S. Zhou, Experimental Observation of Topological Fermi Arcs in Type-II Weyl Semimetal MoTe₂, *Nature Phys.* **12**, 1105 (2016).

- ²² M. M. Hosen, G. Dhakal, B. Wang, N. Poudel, K. Dimitri, F. Kabir, C. Sims, S. Regmi, K. Gofryk, D. Kaczorowski, A. Bansil, and M. Neupane, Experimental Observation of Drumhead Surface States in SrAs₃, *Sci Rep* **10**, 2776 (2020).
- ²³ G. Bian, T.-R. Chang, H. Zheng, S. Velury, S.-Y. Xu, T. Neupert, C.-K. Chiu, S.-M. Huang, D. S. Sanchez, I. Belopolski, N. Alidoust, P.-J. Chen, G. Chang, A. Bansil, H.-T. Jeng, H. Lin, and M. Z. Hasan, Drumhead Surface States and Topological Nodal-Line Fermions in TlTaSe₂, *Phys. Rev. B* **93**, 121113 (2016).
- ²⁴ X. Wang, G. Ding, Z. Cheng, G. Surucu, X.-L. Wang, and T. Yang, Novel Topological Nodal Lines and Exotic Drum-Head-like Surface States in Synthesized CsCl-Type Binary Alloy TiOs, *Journal of Advanced Research* **22**, 137 (2020).
- ²⁵ S. Li, Z.-M. Yu, Y. Liu, S. Guan, S.-S. Wang, X. Zhang, Y. Yao, and S. A. Yang, Type-II Nodal Loops: Theory and Material Realization, *Phys. Rev. B* **96**, 081106 (2017).
- ²⁶ H. Weng, Y. Liang, Q. Xu, R. Yu, Z. Fang, X. Dai, and Y. Kawazoe, Topological Node-Line Semimetal in Three-Dimensional Graphene Networks, *Phys. Rev. B* **92**, 045108 (2015).
- ²⁷ Y.-S. Fu, M. Kawamura, K. Igarashi, H. Takagi, T. Hanaguri, and T. Sasagawa, Imaging the Two-Component Nature of Dirac-Landau Levels in the Topological Surface State of Bi₂Se₃, *Nature Phys* **10**, 815 (2014).
- ²⁸ V. M. Apalkov and T. Chakraborty, Interacting Dirac Fermions on a Topological Insulator in a Magnetic Field, *Phys. Rev. Lett.* **107**, 186801 (2011).
- ²⁹ T. Hanaguri, K. Igarashi, M. Kawamura, H. Takagi, and T. Sasagawa, Momentum-Resolved Landau-Level Spectroscopy of Dirac Surface State in Bi₂Se₃, *Phys. Rev. B* **82**, 081305 (2010).
- ³⁰ P. Cheng, C. Song, T. Zhang, Y. Zhang, Y. Wang, J.-F. Jia, J. Wang, Y. Wang, B.-F. Zhu, X. Chen, X. Ma, K. He, L. Wang, X. Dai, Z. Fang, X. Xie, X.-L. Qi, C.-X. Liu, S.-C. Zhang, and Q.-K. Xue, Landau Quantization of Topological Surface States in Bi₂Se₃, *Phys. Rev. Lett.* **105**, 076801 (2010).
- ³¹ S. K. Chong, R. Tsuchikawa, J. Harmer, T. D. Sparks, and V. V. Deshpande, Landau Levels of Topologically-Protected Surface States Probed by Dual-Gated Quantum Capacitance, *ACS Nano* **14**, 1158 (2020).
- ³² X. Yuan, Z. Yan, C. Song, M. Zhang, Z. Li, C. Zhang, Y. Liu, W. Wang, M. Zhao, Z. Lin, T. Xie, J. Ludwig, Y. Jiang, X. Zhang, C. Shang, Z. Ye, J. Wang, F. Chen, Z. Xia, D. Smirnov, X. Chen, Z. Wang, H. Yan, and F. Xiu, Chiral Landau Levels in Weyl Semimetal NbAs with Multiple Topological Carriers, *Nat Commun* **9**, 1854 (2018).
- ³³ D. R. Saykin, K. S. Tikhonov, and Ya. I. Rodionov, Landau Levels with Magnetic Tunneling in a Weyl Semimetal and Magnetoconductance of a Ballistic $p-n$ Junction, *Phys. Rev. B* **97**, 041202 (2018).
- ³⁴ H. B. Nielsen and M. Ninomiya, The Adler-Bell-Jackiw Anomaly and Weyl Fermions in a Crystal, *Physics Letters B* **130**, 389 (1983).
- ³⁵ E. Benito-Matias, R. A. Molina, and J. Gonzalez, Surface and Bulk Landau Levels in Thin Films of Weyl Semimetals, *Phys. Rev. B* **101**, 085420 (2020).
- ³⁶ Y. Zhang, D. Bulmash, P. Hosur, A. C. Potter, and A. Vishwanath, Quantum Oscillations from Generic Surface Fermi Arcs and Bulk Chiral Modes in Weyl Semimetals, *Sci Rep* **6**, 23741 (2016).
- ³⁷ C. M. Wang, H.-P. Sun, H.-Z. Lu, and X. C. Xie, 3D Quantum Hall Effect of Fermi Arcs in Topological Semimetals, *Phys. Rev. Lett.* **119**, 136806 (2017).
- ³⁸ S. Y. Zhou, G.-H. Gweon, A. V. Fedorov, P. N. First, W. A. De Heer, D.-H. Lee, F. Guinea, A. H. Castro Neto, and A. Lanzara, *Nat. Mater.* **6**, 770 (2007).
- ³⁹ M. A. Vozmediano, M. Katsnelson, and F. Guinea, *Phys. Rep.* **496**, 109 (2010).
- ⁴⁰ B. Amorim, A. Cortijo, F. De Juan, A. Grushin, F. Guinea, A. Gutiérrez-Rubio, H. Ochoa, V. Parente, R. Roldán, P. San-Jose et al., *Phys. Rep.* **617**, (2016).
- ⁴¹ G. G. Naumis, S. Barraza-Lopez, M. Oliva-Leyva, and H. Terrones, *Rep. Prog. Phys.* **80**, 096501 (2017).
- ⁴² H. L. Calvo, H. M. Pastawski, S. Roche, and L. E. F. F. Torres, *Appl. Phys. Lett.* **98**, 232103 (2011).
- ⁴³ G. Usaj, P. M. Perez-Piskunow, L. E. F. Foa Torres, and C. A. Balseiro, *Phys. Rev. B* **90**, 115423 (2014).
- ⁴⁴ Tanay Nag, Anirudha Menon, and Banasri Basu, Thermoelectric transport properties of Floquet multi-Weyl semimetals, *Phys. Rev. B* **102**, 014307 (2020).
- ⁴⁵ Calvin Jerome Tabert, *Electronic Phenomena in 2D Dirac-like Systems: Silicene and Topological Insulator Surface States*, The University of Guelph.
- ⁴⁶ E.H. Sondheimer and A.H. Wilson, *Proc. Roy. Soc.London* **210**, 273 (1951).
- ⁴⁷ A.H. Wilson *Theory of Metals*, [Cambridge UP , Sec 6.6 (1965)].